Author(s): Kousar, Ayesha; Quliyeva, Ulviyya; Pande, Ishan; Sainio, Jani; Julin, Jaakko; Sajavaara, Timo; Jiang, Hua; Laurila, Tomi

Title: Ni Drastically Modifies the Microstructure and Electrochemistry of Thin Ti and Cr Layers

Year: 2024

Version: Published version

Please cite the original version:

Kousar, A., Quliyeva, U., Pande, I., Sainio, J., Julin, J., Sajavaara, T., Jiang, H., & Laurila, T. (2024). Ni Drastically Modifies the Microstructure and Electrochemistry of Thin Ti and Cr Layers. Journal of Physical Chemistry C, 128(3), 1457-1468. https://doi.org/10.1021/acs.jpcc.3c07221

THE JOURNAL OF PHYSICAL CHEMISTRY C
A JOURNAL OF THE AMERICAN CHEMICAL SOCIETY

pubs.acs.org/JPCC
Article

Ni Drastically Modifies the Microstructure and Electrochemistry of Thin Ti and Cr Layers

Ayesha Kousar, Ulviyya Quliyeva, Ishan Pande, Jani Sainio, Jaakko Julin, Timo Sajavaara, Hua Jiang, and Tomi Laurila*

Cite This: J. Phys. Chem. C 2024, 128, 1457−1468

Read Online

ACCESS | Metrics & More | Article Recommendations | Supporting Information

ABSTRACT: There is a significant lack of literature addressing changes in the microstructure of different interfacial metal layer combinations employed in fabricating electrochemical sensors based on carbon nanomaterials. This research gap extends to analyzing their influence on the electrochemical performance, which, in turn, impacts the understanding of the properties of materials incorporating these layers. In this study, microstructural variations and electrochemical activity of chromium and titanium adhesion layers, in combination with nickel catalyst layers (designated as TiNi and CrNi), on silicon wafers were analyzed post annealing. Interestingly, during a brief annealing period of 5 min, TiNi developed a surface layer comprising graphitic carbon, alongside the formation of TiO_2, TiC, and NiSi, and exhibited electrochemical activity toward both dopamine (DA) and ascorbic acid (AA). Conversely, CrNi annealed for 5 min did not show the presence of such a carbon layer and displayed no discernible electrochemical activity toward the target molecules. Only after an extended annealing time of 20 min, signs of a carbon layer appear on CrNi, displaying a moderate electrochemical activity toward DA and AA. The formation of a carbon layer on CrNi is delayed due to the presence of Ni near the surface, which disrupts the local equilibrium. Consequently, the formation of the Cr_2O_3 barrier layer is delayed, which in turn permits carbon diffusion into the underlying Cr layer. Conversely, Ni stabilizes the β-Ti form and markedly decreases the solubility of carbon and oxygen within the TiNi system. By providing a comprehensive analysis of microstructural changes and their impact on the surface chemistry and electrochemical responses of commonly used interfacial metal layers, this paper offers invaluable insights in selecting suitable adhesion and catalyst layer combinations for carbon nanomaterial fabrication.

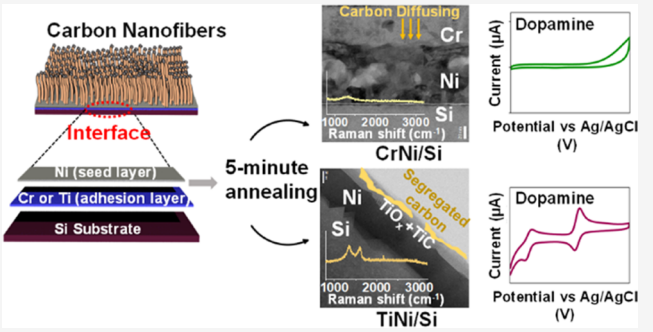

1. INTRODUCTION

Thin layers of Cr and Ti as adhesion layers covered by Ni as catalyst layer are among the commonly used interfacial metal stacks for growing carbon nanofibers (CNFs), graphene, nanowires, and semiconductor nanoparticles finding applications in various areas.[1−4] For growing carbon nanofibers, Ni provides the growth and nucleation sites[5] through its surface step-edge sites acting as preferential growth centers for graphene layers and is known to act best as a catalyst at 600−700 °C.[6,7] Ti and Cr provide better adhesion capability by chemically binding with the substrate and through electrical contact owing to their partially filled d-orbital.[8] Well known for their remarkable electrochemical sensing properties of biomolecules,[9,10] CNFs facilitate chemical interactions with the target molecules (ISR probes); nonetheless, the electrode's electrochemical activity originates from both CNFs and interfacial metal layers. Unfortunately, the role of the interface in determining the electrochemical performance of CNF (and other) electrodes is often overlooked, with the electrochemical properties of the electrodes typically associated only with those of CNFs. Therefore, comprehending the impact of changes in the microstructure of the different seed and adhesion layer combinations on the electrochemical properties of carbon-based sensors is of utmost significance in designing these biosensors with optimized performance.

We have shown in the previous report[11] that (i) in the case of Cr/Si thin layers, surface segregation of carbon induces electrochemical activity. This is a result of (a) the formation of Cr_2O_3, which inhibits the diffusion of carbon uniformly throughout the films and (b) the low solubility of graphite to Cr_2O_3. The combined effect of these two factors leads to the observed surface segregation and subsequent electrocatalytic activity. (ii) In the case of Ti/Si, these phenomena did not take place, as both oxygen and carbon were distributed throughout the Ti film with no or negligible surface segregation. The

Received: October 31, 2023
Revised: January 3, 2024
Accepted: January 5, 2024
Published: January 16, 2024

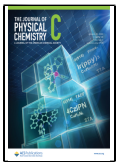

https://doi.org/10.1021/acs.jpcc.3c07221
J. Phys. Chem. C 2024, 128, 1457−1468

presence of a Ni catalyst layer on top of the adhesion layers is essential for the growth of CNFs,[12] for instance. Hence, to obtain a more realistic representation of the interface, here we studied the more complex interfacial systems, i.e., Cr/Ni and Ti/Ni. Due to the varying inherent solubility profiles of common interstitial solutes (O, C, and N) in the Ni seed layer compared to those of Ti and Cr,[13−16] the presence of Ni will cause microstructural changes, likely leading to significant changes in their electrochemistry. These changes will not only affect the growth kinetics of CNFs[1] but also promote/demote the formation of specific phases considered favorable for the EC activity. Despite the importance of the microstructural changes of the interface in the assessment of the structure−property relationships for carbon-based electrodes, there is a lack of information about these changes and their subsequent effects on the electrochemical properties.

Conducting a systematic examination of the surface chemistry at the interface in the presence of CNFs presents a practical challenge. Their extensive coverage impedes accurate measurements and renders them virtually unfeasible. Consequently, it becomes essential to independently investigate changes in the microstructure of the interfacial metal systems, excluding CNFs from the analysis in order to obtain the crucial insights that are otherwise unattainable. Therefore, in this study, we deposited Ni as a catalyst layer on top of commonly used Ti and Cr adhesion layers on silicon substrates to form CrNi (80 nm of Cr and 20 nm of Ni) and TiNi (20 nm of Ti and 20 nm of Ni) substrates commonly used for growing carbon nanofibers.[1,9] These metal layers were annealed at 600 °C for 5 (TiNi-5, CrNi-5) and 20 min (TiNi-20, CrNi-20) in a PECVD chamber (excluding the use of reactive gases and plasma) to mimic the typical ambient conditions during CNF growth.[1,17] We then studied the microstructural changes of these commonly used interfacial metal stacks as a result of annealing and attempted to correlate these with their electrochemical activity toward DA and AA. We found that the presence of Ni drastically modifies the microstructure, surface chemistry, and electrochemical activities of Ti and Cr adhesion layers in comparison to that observed in the previous study.[11] Our findings provide a thorough examination of how the Ni catalyst layer alters the microstructure of the Ti and Cr adhesion layers, consequently affecting surface chemistry and electrochemical characteristics. These insights shed light on the significant role of interface chemistry in determining the electrochemical properties of systems incorporating these layers. This knowledge assists in making informed choices when selecting interfaces for the fabrication of carbon nanomaterial electrodes.

2. METHODS

2.1. Annealing Process. The samples underwent annealing within a chemical vapor deposition (CVD) reactor (Aixtron Black Magic). For this annealing process, the CVD functionality was disabled, utilizing solely the heating function. Following sample loading, the chamber was evacuated by pumping. Subsequently, the temperature was incrementally raised, reaching 395 °C at a rate of 250 °C per minute. It was then further increased to 600 °C at a rate of 300 °C per minute. The annealing duration was either 5 or 20 min at 600 °C. Throughout the annealing process, the chamber was maintained at a pressure of 0.05−0.07 mbar. Following annealing, argon (Ar) was introduced into the chamber, and subsequent cooling brought the temperature down to 150 °C. Ultimately, the samples were extracted from the chamber.

2.2. X-ray Photoelectron Spectroscopy (XPS). XPS was carried out with a Kratos Axis Ultra spectrometer with monochromated Al Kα radiation, a pass energy of 40 eV, an X-ray power of 75 W, and an analysis area of approximately 700 μm × 300 μm. The binding energy scale was based on instrument calibration and no additional binding energy correction was applied to the data. The elemental composition was determined from peak areas of high-resolution core-level spectra after Shirley background subtraction using equipment-specific sensitivity factors. Peak fitting was done using Gaussian−Lorentzian peaks (GL (30) line shape in CasaXPS) with the positions of the peaks fixed to within ±0.1 eV of given binding energies. For sp^2 carbon, an asymmetric line shape was used in CasaXPS.[18] The full widths at half-maximum (fwhm's) of the peaks were restricted to be equal within a fit (excluding the sp^2 carbon peak).

2.3. Raman Spectroscopy. Raman spectroscopy was conducted using a micro-Raman spectroscope (WITec Alpha RA+), which was equipped with an optical microscope. For the measurements, a 50× objective lens and a laser with an excitation wavelength of 532 nm were utilized. Each spectrum was obtained by capturing 10 accumulations with an integration time of 2 s.

2.4. High-Resolution Transmission Electron Microscopy (HR-TEM). TEM imaging was performed on a Jeol JEM 2200FS transmission electron microscope equipped with an X-ray energy dispersive spectrometer (EDS). Cross-sectional TEM samples were prepared by focused ion beam (FIB).

2.5. Conductive Atomic Force Microscopy (C-AFM). C-AFM experiments were conducted using the Jupitor-XR AFM setup with an Asylum electrolever tip. The tip had a conductive coating of Ti/Ir with a spring constant of 2.8 N/m. The samples were attached to the stage by using a magnetic puck and secured with carbon tape. During the experiments, a bias of 3 V was applied to the tip. The measurement area was 5 μm × 5 μm.

2.6. Time-of-Flight Elastic Recoil Detection Analysis (ToF-ERDA). The samples were analyzed with ToF-ERDA using a 13.6 MeV $^{79}Br^{7+}$ ion beam. The angle between the sample normal and the incoming beam was 70° (mirror geometry), while the scattering angle was 40.6°. The analysis was done using Potku,[19] the depth profiles are created by calculating the depth of origin for each recoil based on the recoil energy (ToF) and experimental details. The initial guess of the composition is improved iteratively, yielding the final depth profile in a few iterations. The depth profiles are broadened by the system resolution and, e.g., multiple scattering. This procedure also assumes a laterally homogeneous sample over the 3 mm × 3 mm beam spot; deviations from ideal due to, e.g., roughness or film thickness variation also appear as broadening of the depth profiles.

2.7. Grazing Incidence X-ray Diffraction (GIXRD). Thin films were analyzed with a Rigaku Smartlab diffractometer at the OtaNano Center, Aalto University. Smartlab RIGAKU has a rotating anode X-ray goniometer with a Cu X-ray source (45 kV and 200 mA). The wavelength employed was the copper K-α1 wavelength (λ = 1.541 Å). The instrument was operated at the grazing incidence mode at room temperature, where the incidence slit (IS) was calculated based on the critical angle found from the X-ray reflection measurement. The following equation was used: IS = FP × (sin ω) where FP is the sample's

https://doi.org/10.1021/acs.jpcc.3c07221
J. Phys. Chem. C 2024, 128, 1457−1468

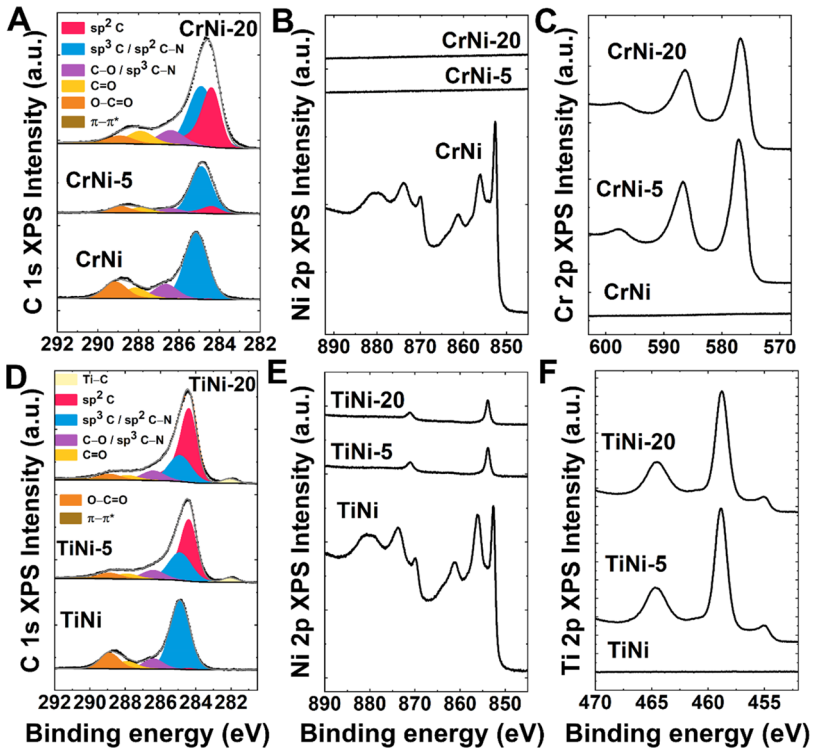

Figure 1. XPS analysis of CrNi and TiNi before and after annealing for 5 and 20 min indicating (A, D) C 1s region, (B, E) Ni 2p region, (C) Cr 2p region, and (F) Ti 2p region.

footprint and ω is the critical angle. The optics configuration utilized was PB (parallel beam) with a limiting slit of 5 or 10 mm, incident slit box, receiving slits of 20.1 mm, and a 2D hybrid pixel detector in 1D mode. X-ray fluorescence reduction mode was used. The 2θ range data was collected from 20 to 100° with a scan step of 0.1°. To avoid forbidden Si peaks, a phi of 8−10° was used. No background correction is done to the data.

2.8. Electrochemistry. Electrochemical measurements were performed by using conventional cyclic voltammetry (CV). A Gamry reference potentiostat was employed, and a three-electrode setup was used comprising a Ag/AgCl reference electrode and a platinum wire as the counter electrode for the electrochemical measurements. Prior to the measurements, the solutions were purged with N_2 gas for 10 min. For each electrochemical measurement, newly prepared electrodes with a radius (r) of 3 mm were utilized. The uncompensated resistance (Ru) was determined for each electrode in phosphate-buffered saline (PBS). The composition of PBS solution is given elsewhere.[10] To evaluate the electrochemical activity of the electrodes in the PBS solution, dopamine hydrochloride (Sigma-Aldrich) and ascorbic acid (AA) from Merck were used. The average values and standard deviations of 3−4 samples are provided.

3. RESULTS

3.1. XPS. High-resolution XPS was employed to study the changes in the chemical composition within the surface region at depths of just a few nanometers. Figure 1 presents the carbon 1s, nickel 2p spectra, Cr 2p and Ti 2p spectra of CrNi and TiNi annealed and as-deposited thin layers. Spectra for other elements, the atomic concentrations, and survey spectra are provided in the Supporting Information (Table S1, Figures S1 and S2).

In the spectra of CrNi and TiNi as-deposited films, noticeable similarities emerge, suggestive of the presence of Ni, NiO, and $Ni(OH)_2$.[20,21] Initially, nickel dominates the surface, but annealing subsequently exposes chromium or titanium depending on the system. Additionally, annealing brings about changes in the carbon species found on the surface. The C 1s spectra in both systems were fitted with seven components: Ti−C (titanium carbide, 282.0 eV), sp^2 carbon (284.5 eV), sp^3 carbon (285.0 eV, which includes contributions from sp^2 C−N bonds), C−O−C and/or C−OH (286.5 eV, potentially containing contributions from sp^3 C−N bonds), C═O (288.0 eV), O−C═O (289.0 eV), and a p−p* shakeup transition (290.9 eV)[22,23] (Table S1). Because of the complexity and high number of possible components, the peak fitting should be considered somewhat tentative, especially for the components with smaller concentrations.

The C 1s spectra show a higher sp^2 content in CrNi-20 compared to CrNi-5 and as-deposited CrNi, however, the shift is less pronounced compared to TiNi-5 (Figure 1A). In CrNi-20, a chromium $2p_{3/2}$ peak around 576.8 eV is attributable to Cr_2O_3[18] (Figure 1C). The Cr $2p_{3/2}$ binding energy is slightly lower in CrNi-5 min than in CrNi-20 min, possibly indicating the presence of $CrO_2/Cr(OH)_3$.[24,25] There is also a N 1s peak observed for these samples at roughly 397 eV (Figure S1) which can be assigned to chromium nitride.[18] This nitride is not readily observed in the Cr 2p spectra because of its low amount.

In the case of TiNi, the C 1s spectra indicate a significant increase in the sp^2 content in TiNi-5 and TiNi-20 compared to as-deposited TiNi (Figure 1C). In the Ti 2p region, a $2p_{3/2}$ peak observed at 458.8 eV indicates the presence of TiO_2. Additionally, a newly emerged $2p_{3/2}$ peak at 455 eV in TiNi-5 and TiNi-20 suggests the formation of titanium carbide as a result of annealing[18] (Figure 1F). A minute and distinct Ni

https://doi.org/10.1021/acs.jpcc.3c07221
J. Phys. Chem. C 2024, 128, 1457−1468

$2p_{3/2}$ peak at 853.8 eV (Figure 1E) together with the emergence of a Si $2p_{3/2}$ peak at 99.5 eV (Figure S2) indicates the formation of nickel silicide.[26] The O 1s spectra indicate the presence of TiO_2 alongside SiO_2 on the surface (Figure S2).

3.2. Raman Spectroscopy. Raman spectroscopy was carried out to study the nature and electronic structure of the carbon layer observed in the surface region of annealed films in the XPS results (Figure 2). CrNi and TiNi before annealing showed a weak band at 525 cm^{-1} characteristic of a typical NiO_x layer on metallic Ni surfaces.[27] In 5 min annealed CrNi films (Figure 2A), a strong signal at 667 cm^{-1} is observed which indicates the presence of a highly disordered surface layer of CrO_2 (the B_{2g} mode at a wavenumber of 686 cm^{-1} in a perfect CrO_2 crystal).[28,29] A small shoulder at 553 cm^{-1} demonstrating the presence of Cr_2O_3 is also observed indicating the mixture of CrO_2 and Cr_2O_3 phases in CrNi-5. In CrNi-20, a sharp band at 649 cm^{-1} is observed which is characteristic of Cr−O stretching vibrations in Cr_2O_3. These results point toward the likely transformation of the CrO_2 phase formed during the initial phase into Cr_2O_3 as a result of increased annealing time.[29] It is worth mentioning that the fwhm of the Cr_2O_3 peak in CrNi-20 is about 258 cm^{-1} whereas in CrNi-5 films it is measured to be 163 cm^{-1}. This corresponds to the shorter phonon lifetime when interacting with the incident photon in the former case indicating the amorphous nature of Cr_2O_3.[30] A broad peak around 1322 cm^{-1} is observed on CrNi-5, indicating the presence of a thin carbon layer. This indicates the existence of carbon atoms in the sample, likely due to contamination or residual carbon during the fabrication. In CrNi-20, a G peak appears at 1554 cm^{-1} in addition to a D peak at 1355 cm^{-1}. The presence and position of the G band at 1554 cm^{-1} indicates the existence of amorphous carbon with a high content of structural defects.[31,32]

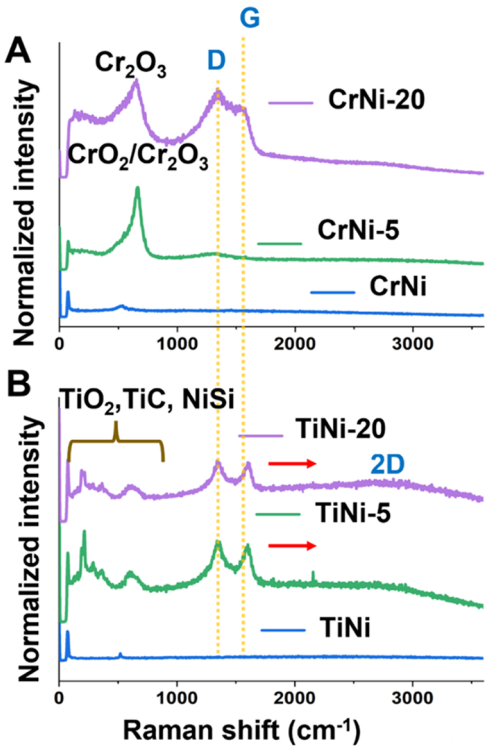

Figure 2. Raman spectra of (A) CrNi and (B) TiNi before and after annealing.

Interestingly, in the case of TiNi annealed films (Figure 2B), sharp peaks D and G and a broad 2D peak are observed at 1355, 1603, and 2800 cm^{-1} even after five min of annealing. The presence of G peak at ∼1600 cm^{-1} and broad 2D peaks indicate the presence of layered nanocrystalline graphitic structures with a fair amount of defects.[33,34] Both TiNi-5 and TiNi-20 showed bands at 193, 214, and 398 indicative of anatase structure, and the band at 609 cm^{-1} is indicative of the rutile phase of TiO_2.[35] This indicates that the mixture of both phases, i.e., anatase and rutile, is present. Moreover, the presence of TiC and NiSi is also indicated by the bands at 256 and 286, and at 368 cm^{-1} respectively.[36−38]

3.4. HR-TEM. Cross-sectional HR-TEM images (Figure 3) indicate the presence of crystalline regions in addition to a few amorphous regions on the surface of CrNi-5 films. In this case, the Ni atoms diffuse through the Cr layer, and there is no indication of Ni left on the surface (first few nanometers) according to the EDS line scans and elemental mapping (Figures S3 and S4). However, some Ni can be seen within 20 nm of the surface in the EDS scans. Some of the Ni has already reached the underlying Si, resulting in the formation of Ni silicides. A solid solute ion of Cr and Ni can be seen in the TEM images. The interatomic spacing (*d*-spacing) of the crystalline regions was measured. HR-TEM of CrNi-5 shows 0.22 nm *d*-spacing in the visible lattice planes which can be associated with the presence of Cr_2O_3 (110)[39] (Figure 3E). Nonetheless, the *d*-spacing of (101) CrO_2 is also reported to be in a similar range i.e., 0.24 nm.[40] Additionally, these crystalline regions exhibit nonuniform distribution and appear to comprise a mixture of phases. In CrNi-20, Ni reaches the Si substrate, forming grains of Ni and Cr that appear to be segregated. There is no indication of Ni present within 20 nm of the surface (Figure 3D). However, some Ni suspended toward the middle of the Cr film can be seen in the TEM micrograph (Figure 3C,D). The surface region does not show any crystalline region and the surface is amorphous. The amorphous nature of the Cr_2O_3 was also indicated by Raman spectra where Cr_2O_3 peaks with wider fwhm were observed (Figure 2A).

In the TiNi case, after annealing for 5 min, all of the Ni diffuses completely to the Ti layer and Si substrate forming a mixture of phases. The surface region contains a few amorphous areas in addition to the crystalline regions. Interestingly, a layer of amorphous region is formed beneath the crystalline region (Figure 3H). EDS map showed that the crystalline region toward the surface is rich with Ti, while the underneath amorphous layer contains high amounts of Si, Ni, carbon, and oxygen in addition to Ti (Figures S5A and 3J). The presence of the amorphous layer is pointing toward the occurrence of interfacial reactions in multilayer thin film systems involving a high amount of oxygen, carbon, and nitrogen.[41,42] The presence of carbon is verified by the EDS scan (Figure 3J). Calculated values of lattice plane spacings (Figure 3I) pointed toward the presence of TiO_2, TiC, and NiSi on/near the surface.[43−45] However, these HR-TEM micrographs did not show the presence of graphite lattice planes, even though Raman spectroscopy and XPS indicated high sp^2 content on the surface. Ni supports the formation of TiC, which contrasts with the behavior observed in the CrNi system. The isothermal section of the Cr−Ni−C phase diagram[46] shows that as Ni starts to be alloyed with Cr, the

https://doi.org/10.1021/acs.jpcc.3c07221
J. Phys. Chem. C 2024, 128, 1457−1468

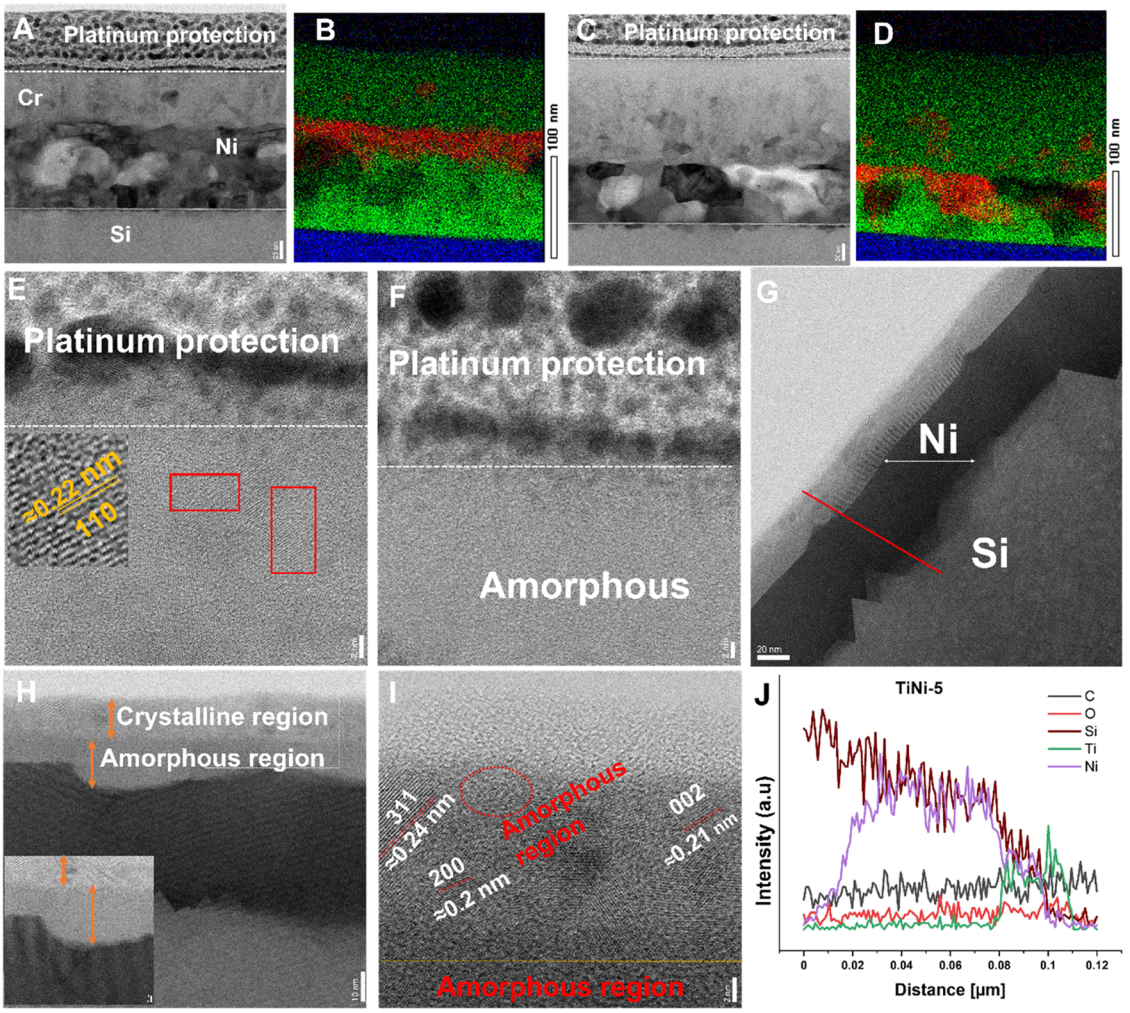

Figure 3. TEM and EDS mapping. (A) CrNi-5 and (B) EDS map of CrNi-5 (green: Cr, blue: Si, red: Ni). (C) CrNi-20 and (D) EDS map of CrNi-20. (E) HR-TEM image of CrNi-5 near surface where red boxes indicate the presence of crystalline regions. (F) HR-TEM image of CrNi-20 near surface. (G) TEM image of TiNi-5 (H) and (I) HR-TEM images of TiNi-5 showing TiO_2 (311), NiSi (002), and TiC (200). (J) EDS line scan (red line in G) of TiNi-5.

sequential formation of Cr-carbides can take place. When the Ni content crosses the solubility limit of Ni in bcc-Cr, two-phase equilibrium between Cr and $Cr_{23}C_6$ becomes possible. Despite this, there is no indication of CrC formation in CrNi annealed films even after almost complete depletion of Ni from the surface area[46] emphasizing the metastable equilibria in the system.

3.5. GIXRD. GIXRD analysis of pristine CrNi and TiNi shows the presence of Ni and NiO on the surface[47] (Figure 4A). GIXRD of Ti and Cr films is also provided to assess the phases associated with the underlying metals (Figure 4B). Both Cr and Ti contain a mixture of oxides and metallic forms. TiNi-5 and TiNi-20 films (Figure 4C) show the presence of TiO_2, NiSi, TiC, and SiC.[48−51] A peak corresponding to 002 graphite[52] is also observed on TiNi-5 and TiNi-20. CrNi-5 shows (Figure 4D) the presence of Cr_2O_3 in addition to CrN on the surface.[53,54] CrNi-20 films exhibit the presence of Cr_2O_3 and other phases, similar to what is observed in CrNi-5. However, it is worth noting that the peaks in the CrNi-20 case exhibit a slightly broader profile compared to those in the CrNi-5 case. GIXRD was unable to detect graphite in CrNi-20, which was evident in Raman spectra and XPS analysis, likely because this graphite layer is confined to only the first few nanometers of the films.

3.6. C-AFM. Conductive AFM measurements were carried out to evaluate the differences in the surface morphology and electron transport properties of interfaces in the *z*-direction. C-AFM is a form of scanning probe technique that simultaneously measures the surface topography and the local conductivity with nanometer-scale resolution.[55] The 3D topography of 5 min annealed CrNi films (Figure 5A) showed rodlike nanostructures on the surface with grain sizes in the range of ∼50 nm. The appearance of the grains is due to the crystalline structure of the CrNi-5 films (Figure 5D) verified by XRD (Figure 4). The corresponding current images show the conductive nature of these rodlike nanostructures. The surface of 20 min annealed CrNi films did not show clearly defined grains, and the surface geometries are random unlike in the case of CrNi-5 (Figure 5B,E). This could be due to the amorphous nature of the surface as indicated by the TEM, XRD, and Raman spectroscopy. The current image of CrNi-20 indicates that the surface is not entirely conductive, but there are some random conductive patches (Figure 5G). The conductance of these random patches is significantly higher than the 5 min annealed surface. These conductive patches are

https://doi.org/10.1021/acs.jpcc.3c07221
J. Phys. Chem. C 2024, 128, 1457−1468

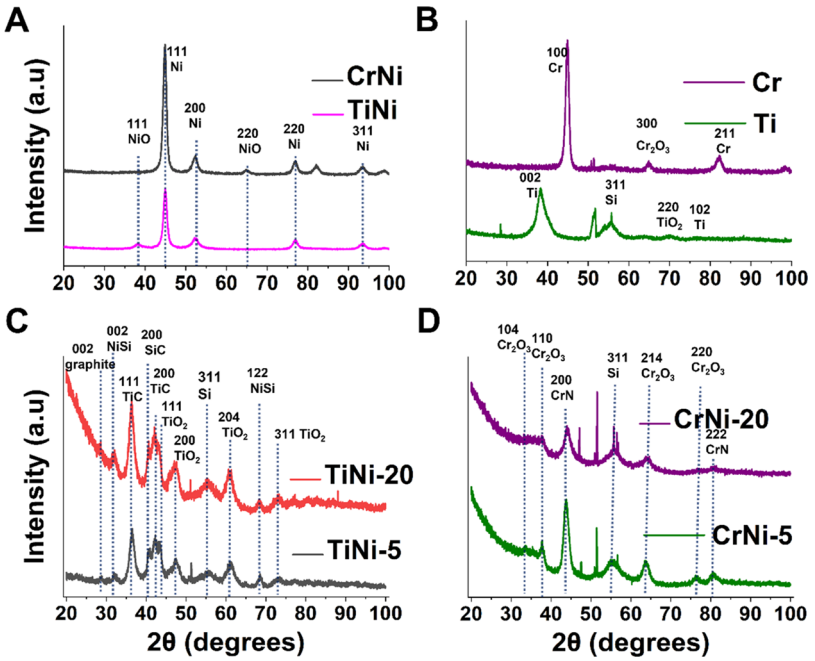

Figure 4. GIXRD analysis of (A) as-deposited CrNi and TiNi and (B) Cr and Ti on a silicon substrate. (C) TiNi and (D) CrNi after 5 and 20 min of annealing.

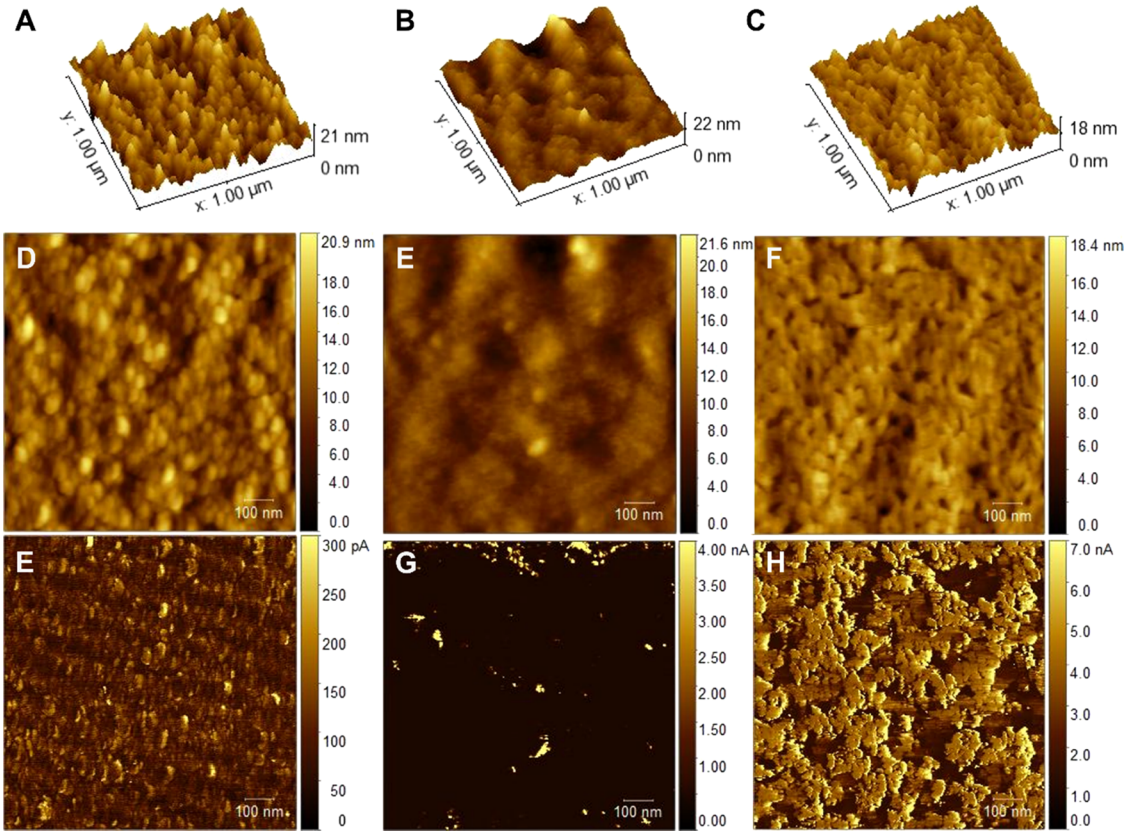

Figure 5. C-AFM micrographs with 3D topography and current images for (A, D, E) CrNi-5, (B, E, G) CrNi-20, and (C, F, H) TiNi-5. Applied bias: 1 V.

most likely surface-segregated carbon. In the case of TiNi-5 films, the 3D topography indicates a mostly crystalline surface, interspersed with occasional darker patches, signifying nonuniform topography (Figure 5C,F). This suggests the presence of a disordered layer covering the surface, varying in thickness. The corresponding current image (Figure 5H) indicates that this disordered layer is highly conductive, while the underlying region shows lesser conductance. It is worth mentioning that the boundaries of the patches of this layer are elevated and conduct higher current, reaching 38 nA (Figure S5B). We

https://doi.org/10.1021/acs.jpcc.3c07221
J. Phys. Chem. C 2024, 128, 1457−1468

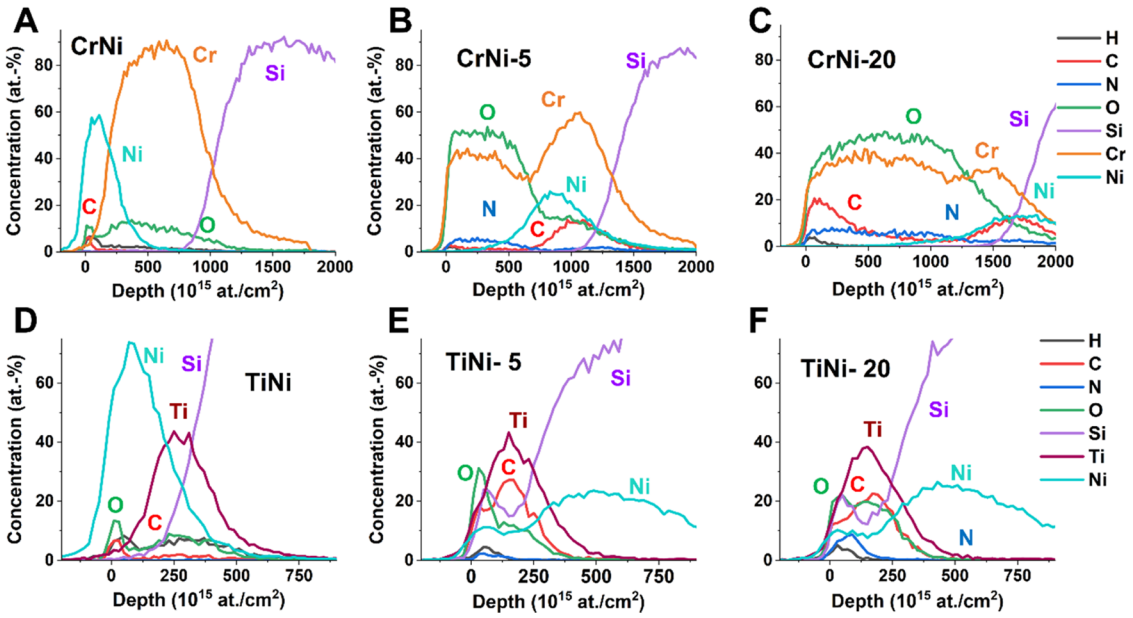

Figure 6. ToF-ERDA depth profiles for (A) CrNi, (B) CrNi-5, (C) CrNi-20, (D) TiNi, (E) TiNi-5, and (F) TiNi-20.

Table 1. Summary of the Phases Formed on Annealed TiNi and CrNi Films, as Indicated by Various Characterization Techniques

materials	overall phases (in the surface region)	XPS	Raman spectroscopy	TEM	GIXRD
CrNi-5	Cr_2O_3, CrO_2, CrN	Cr_2O_3/CrO_2/ $Cr(OH)_3$, CrN	Cr_2O_3, CrO_2	Cr_2O_3/CrO_2	Cr_2O_3, CrN
CrNi-20	Cr_2O_3, CrN, sp^2 carbon	Cr_2O_3, CrN, sp^2 carbon	Cr_2O_3, sp^2 carbon	Amorphous surface	Cr_2O_3, CrN
TiNi-5	TiO_2, TiC, NiSi, SiO_2/SiC, sp^2 carbon	TiO_2, TiC, NiSi, SiO_2, sp^2 carbon	TiO_2, TiC, NiSi, sp^2 carbon	TiO_2, TiC, NiSi	TiO_2, TiC, NiSi, SiC, sp^2 carbon
TiNi-20	TiO_2, TiC, NiSi, SiO_2/SiC, sp^2 carbon	TiO_2, TiC, NiSi, SiO_2, sp^2 carbon	TiO_2, TiC, NiSi, sp^2 carbon		TiO_2, TiC, NiSi, SiC, sp^2 carbon

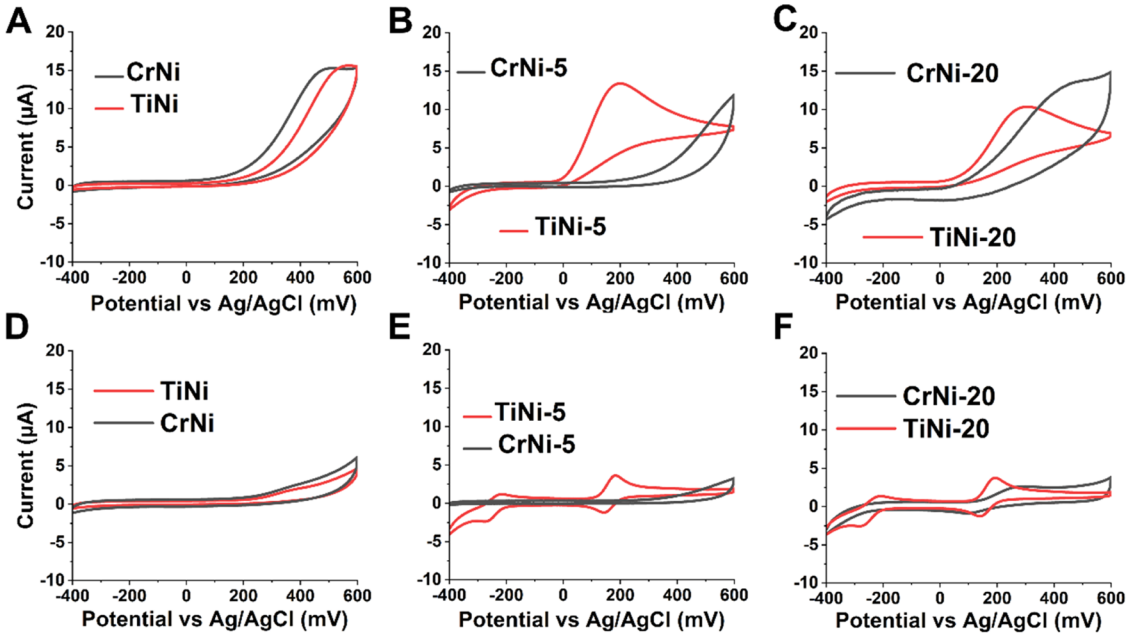

Figure 7. Electrochemistry of (A–C) AA and (D–F) DA on CrNi and TiNi before and after annealing.

capped conductance in the image by 7 nA to make all of the conductive points in the figure visible. The observed valleys of increased conductance most likely correspond to the precipitated graphite, whereas regions with lower conductivity likely correspond to other surface phases observed on TiNi-5.

https://doi.org/10.1021/acs.jpcc.3c07221
J. Phys. Chem. C 2024, 128, 1457−1468

Table 2. Selected Electrochemical Parameters Including Oxidation Peak Current (I_{pa}), Reduction Peak Current (I_{pc}), Oxidation Peak Potential (E_{pa}), Reduction Peak Potential (E_{pc}), Onset Potential, and Peak Separation (ΔE_p) of AA and DA on the As-Deposited and Annealed CrNi and TiNi Electrodes (ν = 100 mV/s)

	100 μM DA						1 mM AA		
electrodes	I_{pa} (μA)	I_{pc} (μA)	E_{pa} (mV)	E_{pc} (mV)	ΔE_p (mV)	onset potential (mV)	I_{pa} (μA)	E_{pa} (mV)	onset potential (mV)
CrNi			354 ± 4					465 ± 4	228 ± 6
CrNi-5	no peak						no peak		
CrNi-20	1 ± 0.1	0.9 ± 0.1	255 ± 33	106 ± 15	149 ± 48	150 ± 12	3.5 ± 1	337 ± 35	49 ± 5
TiNi			348 ± 2					507 ± 2	256 ± 19
TiNi-5	2.66 ± 0.4	1.7 ± 0	189 ± 9	142 ± 4	47 ± 13	124 ± 7	8 ± 1	237 ± 28	33 ± 19
TiNi-20	1.95 ± 0.35	1.4 ± 0.1	199 ± 10	137 ± 2	62 ± 12	128 ± 6	7 ± 1	273 ± 27	57 ± 23

3.7. ToF-ERDA. We employed ToF-ERDA to investigate depth profiles, elemental composition, and distribution in both CrNi and TiNi films before and after annealing (Figure 6). CrNi and TiNi as-deposited layers showed Ni layer covering the underlying Ti and Cr layers (Figure 6A,D). In CrNi 5 min annealed films, we can observe the Ni diffusion profile, which extends deeper into the sample (Figure 6B). Further, in CrNi-20 films, we observe that Ni has diffused even deeper into the sample (Figure 6C). Meanwhile, Cr diffuses outward and reacts with oxygen. Additionally, some carbon is found at a penetration depth as Ni. ERDA results indicate that the depth of the Ni concentration profile is also affecting the Cr and oxygen distribution profiles. Moreover, nitrogen is also present throughout the thickness of the sample. A carbon profile in the form of a "hump" can be seen on the CrNi-20 sample indicating that Cr, O, and N present in the system are forming phases that affect and effectively hinder the diffusion of carbon. XPS, Raman, and GIXRD all support the presence of Cr_2O_3 as well as CrN, both known for their properties as a carbon diffusion barrier.[56] However, Cr_2O_3 appears to be the dominant phase. ERDA results confirm the influence of Ni on Cr and O distributions, which consequently reduces the diffusion of carbon into the thin films.

In the case of TiNi, after 5 min of annealing, Ni has also diffused deeper into the sample (Figure 6E). The distribution of Ni appears to be more uniform and evenly spread throughout the film in this case, unlike in the case of Cr where we observed more localized humps in the Ni concentration profile. In addition to the outward diffusion of Ti and inward diffusion of Ni, Si is also observed to diffuse toward the surface. A significant amount of carbon can be seen near the surface. Furthermore, no significant changes in the elemental distributions are observed in the 20 min annealed TiNi samples compared to TiNi-5, except for a more uniform oxygen distribution in Ti and a slight increase in nitrogen concentration (Figure 6F). A summary of the phases formed on the annealed CrNi and TiNi films, as indicated by all characterization techniques used in this study, is presented in Table 1.

3.8. Electrochemistry. Cyclic voltammetry was carried out to study the electrochemical activity of CrNi and TiNi before and after annealing (Figure 7, Table 2). Inner sphere probes DA and AA were chosen due to their relevance for biosensing applications. The redox reactions of the ISR provide valuable information about the chemical functionalities present on these electrode surfaces. The cyclic voltammograms for AA oxidation on CrNi and TiNi electrodes exhibited a peak around 465−500 mV, indicating the oxidation reaction from ascorbic acid to dehydroascorbic acid. The oxidation potential of AA is fairly anodically shifted than the observed oxidation peak position for CNFs.[10] Similarly in the case of DA, a small peak at approximately 350 mV suggests a limited contribution from the CrNi and TiNi surfaces to the oxidation of DA to DAQ, with no corresponding reduction peak (Figure 7A,D). This points out that the Ni surface present on the Cr and Ti layers shows moderate electrocatalytic properties.

CrNi-5 could not detect either AA or DA. After annealing for 20 min, the CrNi electrode showed improved AA as well as DA oxidation indicated by the AA onset oxidation potential of 49 ± 5 and emergence of both DA oxidation and reduction peaks at 255 ± 33 and 106 ± 15 mV, respectively (Figure 7B,E, Table 2). Therefore, the presence of the sp^2 content is proven to be critical for electrochemical activity. Interestingly, TiNi-5 after being annealed for 5 min showed well-defined oxidation and reduction peaks for DA at 189 ± 9 and 142 ± 4, which are considerably cathodically shifted in comparison to the 20 min annealed CrNi electrode surface. Similarly, TiNi-5 showed AA oxidation at 237 ± 28 mV (Figure 7B,E). The electrochemical activity of 20 min annealed TiNi electrodes also showed well-defined peaks for the DA > DAQ and AA oxidation reactions (Figure 7C,F). The differences in the redox potentials in TiNi-5 and TiNi-20 are within the error bars. This indicates that the surface chemistry of TiNi does not undergo major differences as the annealing time increases from 5 to 20 min. However, slight changes can be due to the possibility of some of the surface carbon being redissolved to TiC + TiO_{1-x} mixed layer as the annealing time is increased.

4. DISCUSSION

The combined findings presented above highlight the presence of various phases on the surfaces of TiNi and CrNi samples after annealing for different durations. Specifically, TiO_2, TiC, NiSi, and graphitic carbon were observed on the TiNi surface after 5 min of annealing. In contrast, the CrNi-5 surfaces lacked the presence of carbides or sp^2-bonded carbon. This implies that in the case of TiNi, sp^2 carbon segregation to the surface occurs earlier compared to CrNi, which is completely opposite to that observed in plain systems Cr and Ti without Ni.[11] Despite titanium's known high carbon and oxygen solubility,[14] the presence of nickel reduces their solubility, leading to carbon segregation on the surface. This phenomenon accelerates carbon and oxygen saturation, resulting in the formation of TiO_2 and TiC. Conversely, chromium appears to dissolve both carbon and oxygen because the presence of nickel significantly delays the formation of surface carbon layers. In a previous study, we demonstrated that annealing increases the solubility of carbon and oxygen in the titanium layer.[11] Notably, nickel fundamentally alters titanium's behavior, promoting the formation of carbides, silicides, and segregated carbon layers, indicating reduced carbon solubility,

https://doi.org/10.1021/acs.jpcc.3c07221
J. Phys. Chem. C 2024, 128, 1457−1468

attributed to nickel acting as a known β-Ti stabilizer (see Ti−Ni binary phase diagram[57]).

Some reports in the literature have demonstrated the electrocatalytic activity of Ni- and Cr-incorporated N-doped CNFs grown on Nichrome foil substrate for the electrochemical detection of urea and trifunctional ORR, OER, and HER activities.[58,59] Nanoparticles of Ni and Cr were introduced into both the trunks and tips of CNFs, resulting in a notable improvement in their electrocatalytic activities. It is worth noting that the investigation presented here involves the utilization of thin layers of Ni on Cr and Ti adhesion layers, deposited on a silicon substrate, for the purpose of growing vertically oriented CNFs.[17] Ni, functioning as a catalyst for CNF growth, initiates the nucleation of fibers, resulting in the formation of tip-grown carbon nanofibers. Some of the Ni diffuses toward the Si substrate due to its pronounced affinity for silicon. Simultaneously, metallic Cr undergoes a transformation into oxides and nitrides, serving the role of anchoring carbon nanofibers to the silicon substrate. Importantly, Cr does not become integrated into the CNFs[17] and does not exhibit any discernible electrocatalytic activity. The incorporation of Ni/NiO into the tips of the CNFs may potentially enhance the electrocatalytic activities. In the case of TiNi annealed electrodes, the presence of TiO_2 and TiC, alongside graphitic carbon, contributes to the electrochemical activity toward both DA and AA. However, the primary source of electrochemical activity stems from carbon nanofibers or carbon that is gettered on top of the substrate. The interfacial metal layers play a crucial role in modulating the carbon segregation process by either decelerating or accelerating it.

The primary reason for the absence of a carbon layer on CrNi-5 lies in the delayed formation of a homogeneous Cr_2O_3 layer when nickel is present. This is because the establishment of a local equilibrium between Cr and Cr_2O_3 cannot occur until Ni has been depleted from the surface region, as depicted in the isothermal section of the Cr−Ni−O phase diagram.[60] As this is a diffusion-driven process, it will require time. As observed in our recent paper,[11] Cr_2O_3 serves as an effective diffusion barrier for carbon, which is not formed in the case of CrNi-5 due to the above-discussed delay. Consequently, carbon can infiltrate deeper into the layers, resulting in a more evenly distributed carbon concentration profile and a reduced tendency for surface segregation. It is widely acknowledged that carbon's solubility in Cr_2O_3 is exceedingly low, if not negligible.[61] Hence, when Cr_2O_3 formation eventually transpires, the majority of the carbon within that volume segregates to the external or internal boundaries. However, due to the lag in the diffusion barrier (Cr_2O_3) formation, most of the carbon has already diffused into the underlying film, leaving only a small portion of the carbon in the surface region available for the segregation process.

Raman spectroscopy, XPS, and GIXRD all indicated the presence of Ni and NiO on the surfaces of as-deposited CrNi and TiNi. The mild electroanalytical activity of CrNi and TiNi films is attributed to the reported electrochemical activity of Ni and NiO toward DA and AA.[62−64] However, after annealing for five min, CrNi-5 did not show any signs of oxidation for either AA or DA. Surface characterization techniques indicated the presence of a mixture of CrO_2, Cr_2O_3, and some disordered carbon. Ni diffusion into the Cr layer and toward the Si substrate was evident, but some dark regions in the HR-TEM image near the surface suggested the presence of some Ni near the surface. However, the distribution of dark and bright spots was nonuniform, indicating the presence of practically Ni-free regions on the surface as well. Based on the isothermal section of the Cr−Ni−O phase diagram,[60] for the formation of Cr_2O_3, the surface region must have a low enough Ni concentration to avoid the formation of the γ phase or a ternary Ni−Cr−O compounds. However, the formation of the γ phase or ternary compounds is unlikely during our short annealing times due to the time required for the nucleation of these ordered structures. Therefore, the formation of the Cr_2O_3 layer is postponed as well. As discussed above, the formation of a uniform Cr_2O_3 layer is needed for the segregation of carbon to the surface, as it acts as a diffusion barrier, preventing uniform carbon distribution through the film.

The formation of segregated ordered carbon on TiNi after just five min of annealing, in contrast to CrNi surfaces, suggests faster kinetics for graphitic carbon formation on TiNi. In addition to the graphitic carbon, the presence of TiO_2, TiC, and NiSi is indicated. Raman spectroscopy indicated the presence of both anatase and rutile phases of TiO_2 on TiNi-5 annealed samples. Moreover, TiNi-5 displayed well-defined oxidation peaks for DA and AA at cathodically shifted potentials compared to CrNi-20. TiNi-20 also displayed well-defined peaks for DA and AA oxidation reactions, indicating comparable surface chemistry to TiNi-5. The presence of layered graphitic carbon on the TiNi-5 is expected to be the biggest contributing factor toward the electrochemically active TiNi-5 surface. However, the anatase phase of TiO_2 is also reported to show good electronic connectivity with the substrate and is considered an excellent electrocatalyst for electrochemical biosensing applications.[65] Likewise, TiC exhibits good chemical stability and electrical conductivity which results in electrochemical activity similar to that of noble metals.[36,66] Based on what has been stated above, the role of TiO_2 and TiC in the observed electrochemical activity cannot be ruled out completely.

Previous reports indicate that the solubility of oxygen in α-Ti is high, whereas in β-Ti, it is notably lower and exhibits a greater dependence on temperature compared to α-Ti.[67,68] Similarly, carbon solubility in β-Ti is lower than that in α-Ti. In Ti alloys, the portion of carbon not dissolved in α-Ti and β-Ti forms titanium carbide[69,70] (see isothermal sections of Ti−Ni−C ternary system[71]). Furthermore, Ni is a known β-stabilizer, reducing the β-transition temperature and potentially stabilizing this phase at room temperature. The reduced solubility of oxygen and carbon in annealed TiNi suggests the presence of some β-Ti phase, which appears to facilitate the formation of TiO_x in addition to TiC. Although there are no signs of β-Ti in the pristine TiNi films, the presence of Ni may favor the α-to-β phase transition during annealing. The formation of TiO_x is only feasible when there is no remaining Ni as shown in the ternary Ni−Ti−O phase diagram.[72] However, Ni diffusion is observed to occur rapidly, as the reaction with the silicon substrate and formation of NiSi are evident in the TEM micrographs after 5 min of annealing. Further, NiSi cannot exist in local equilibrium with Ti (see Ti−Ni−Si ternary phase diagram[73]), so most of the Ni is converted to NiSi, shifting the local equilibrium conditions toward the Ti-rich environment at the surface. As no other Ni-silicide or TiNi compounds were observed at the surface region and because of the low solubility of Ni to Ti, one can expect the surface to be practically depleted from Ni, and we can therefore utilize the isothermal section of the Ti−C−O phase diagram[74] to further analyze the

https://doi.org/10.1021/acs.jpcc.3c07221
J. Phys. Chem. C 2024, 128, 1457−1468

phase relations in the surface region. The isothermal section indicates that TiC shows extensive solubility for O and C at 1473 K. However, despite the extensive solubility range for C and O in TiC[O,C], TiO_x cannot exist at local equilibrium directly with TiC[O,C]. At lower temperatures (873 K), the phase equilibria will shift and the solubility of the O and C will decrease. The above-discussed presence of TiO_x, TiC, and graphitic carbon on TiNi-5 suggests significant deviations from the expected equilibria indicating only local metastable equilibrium conditions in these samples as expected based on their multimaterial nature and short annealing times.

5. CONCLUSIONS

Ti and Cr thin metal layers commonly used as adhesion layers together with the layer of Ni catalyst for growing carbon nanofibers were annealed at 600 °C for the duration of 5 and 20 min in a PECVD chamber (with the absence of plasma and reactive gases) to study the differences in the microstructure and resulting electrochemical properties. Ni affects the microstructural evolution and electrochemical properties of both the Ti and Cr adhesion layers in an opposite way. XPS, Raman spectroscopy, ToF-ERDA, GIXRD, and C-AFM showed the presence of sp^2 carbon in addition to TiO_2, TiC, NiSi, SiO_2/SiC on TiNi after 5 min of annealing. A similar range of phases was observed on TiNi after 20 min of annealing. Cyclic voltammetry results demonstrated that the TiNi interface after 5 min of annealing showed the best electrochemical activities toward DA and AA among all of the electrodes studied. The presence of graphitic carbon in addition to TiO_2 and TiC is responsible for the electrochemical activity. However, CrNi after 5 min of annealing did not show any electrochemical activity. Only after 20 min of annealing, CrNi electrodes showed moderate electrochemical activity toward DA and AA. Phase diagrams and experimental evidence obtained through various characterization techniques indicate that the presence of Ni near the surface postpones the formation of the Cr_2O_3 layer in the CrNi film annealed for 5 min. This delay facilitates the continued diffusion of carbon within the Cr layer. However, following 20 min of annealing, the absence of Ni near the surface becomes apparent, resulting in a more uniform Cr_2O_3 layer compared to 5 min annealed CrNi. This uniformity is a key factor in establishing barrier properties against carbon diffusion. These results point toward the completely different properties of TiNi and CrNi interfacial systems giving rise to different microstructure and surface chemistry and hence completely different electrochemical properties. This work finds significance in selecting proper material combinations for the electrochemical sensor fabrication utilizing interfacial metal layers.

■ ASSOCIATED CONTENT

Supporting Information

The Supporting Information is available free of charge at https://pubs.acs.org/doi/10.1021/acs.jpcc.3c07221.

Additional XPS, AFM, and EDS results for characterizing the materials (PDF)

■ AUTHOR INFORMATION

Corresponding Author

Tomi Laurila − *Department of Electrical Engineering and Automation, School of Electrical Engineering, Aalto University, 00076 Aalto, Finland; Department of Chemistry and Materials Science, School of Chemical Engineering, Aalto University, 00076 Aalto, Finland;* orcid.org/0000-0002-1252-8764; Email: tomi.laurila@aalto.fi

Authors

Ayesha Kousar − *Department of Electrical Engineering and Automation, School of Electrical Engineering, Aalto University, 00076 Aalto, Finland;* orcid.org/0000-0002-0483-2547

Ulviyya Quliyeva − *Department of Electrical Engineering and Automation, School of Electrical Engineering, Aalto University, 00076 Aalto, Finland*

Ishan Pande − *Department of Electrical Engineering and Automation, School of Electrical Engineering, Aalto University, 00076 Aalto, Finland;* orcid.org/0000-0002-0033-5201

Jani Sainio − *Department of Applied Physics, School of Science, Aalto University, 00076 Aalto, Finland*

Jaakko Julin − *Department of Physics, University of Jyväskylä, FI-40014 Jyväskylä, Finland;* orcid.org/0000-0003-4376-891X

Timo Sajavaara − *Department of Physics, University of Jyväskylä, FI-40014 Jyväskylä, Finland*

Hua Jiang − *Department of Applied Physics, School of Science, Aalto University, 00076 Aalto, Finland*

Complete contact information is available at: https://pubs.acs.org/10.1021/acs.jpcc.3c07221

Notes

The authors declare no competing financial interest.

■ ACKNOWLEDGMENTS

The authors acknowledge the provision of facilities and technical support by Aalto University at OtaNano−Nanomicroscopy Center (Aalto-NMC) and Micronova Nanofabrication Centre. Lide Yao is acknowledged for preparing the cross sections for TEM analysis.

■ REFERENCES

(1) Pande, I.; Sainio, S.; Sainio, J.; Liljeström, V.; Jiang, H.; Laurila, T. Correlation between Microstructure and Surface Chemistry of Carbon Nanofibers Grown Using Different Adhesive Layers. *Diamond Relat. Mater.* **2023**, *133*, No. 109713.

(2) Kim, H.; Lee, S.; Shin, J.; Zhu, M.; Akl, M.; Lu, K.; Han, N. M.; Baek, Y.; Chang, C. S.; Suh, J. M.; et al. Graphene Nanopattern as a Universal Epitaxy Platform for Single-Crystal Membrane Production and Defect Reduction. *Nat. Nanotechnol.* **2022**, *17* (10), 1054−1059.

(3) Singh, A. P.; Roccapriore, K.; Algarni, Z.; Salloom, R.; Golden, T. D.; Philipose, U. Structure and Electronic Properties of InSb Nanowires Grown in Flexible Polycarbonate Membranes. *Nanomaterials* **2019**, *9* (9), 1260.

(4) Madhankumar, P.; Sujatha, L.; Sundar, R.; Viswanadam, G. Fabrication of Low-Cost MEMS Microfluidic Devices Using Metal Embossing Technique on Glass for Lab-on-Chip Applications. *J. Micromech. Microeng.* **2023**, *33* (8), 084001.

(5) Vishwakarma, R.; Shinde, S. M.; Rosmi, M. S.; Takahashi, C.; Papon, R.; Mahyavanshi, R. D.; Ishii, Y.; Kawasaki, S.; Kalita, G.; Tanemura, M. Influence of Oxygen on Nitrogen-Doped Carbon Nanofiber Growth Directly on Nichrome Foil. *Nanotechnology* **2016**, *27* (36), No. 365602.

(6) Abild-Pedersen, F.; Nørskov, J. K.; Rostrup-Nielsen, J. R.; Sehested, J.; Helveg, S. Mechanisms for Catalytic Carbon Nanofiber Growth Studied by Ab Initio Density Functional Theory Calculations. *Phys. Rev. B* **2006**, *73* (11), No. 115419.

(7) Lyu, Y.; Wang, P.; Liu, D.; Zhang, F.; Senftle, T. P.; Zhang, G.; Zhang, Z.; Wang, J.; Liu, W. Tracing the Active Phase and Dynamics for Carbon Nanofiber Growth on Nickel Catalyst Using Environmental Transmission Electron Microscopy. *Small Methods* **2022**, *6* (6), No. 2200235.
(8) Abbott, W. M.; Murray, C. P.; Ní Lochlainn, S.; Bello, F.; Zhong, C.; Smith, C.; McCarthy, E. K.; Downing, C.; Daly, D.; Petford-Long, A. K.; et al. Comparison of Metal Adhesion Layers for Au Films in Thermoplasmonic Applications. *ACS Appl. Mater. Interfaces* **2020**, *12* (11), 13503−13509.
(9) Sainio, S.; Palomäki, T.; Tujunen, N.; Protopopova, V.; Koehne, J.; Kordas, K.; Koskinen, J.; Meyyappan, M.; Laurila, T. Integrated Carbon Nanostructures for Detection of Neurotransmitters. *Mol. Neurobiol.* **2015**, *52* (2), 859−866.
(10) Kousar, A.; Pande, I.; F Pascual, L.; Peltola, E.; Sainio, J.; Laurila, T. Modulating the Geometry of the Carbon Nanofiber Electrodes Provides Control over Dopamine Sensor Performance. *Anal. Chem.* **2023**, *95* (5), 2983−2991.
(11) Kousar, A.; Quliyeva, U.; Pande, I.; Sainio, J.; Julin, J.; Sajavaara, T.; Karttunen, A. J.; Laurila, T. Enhancing Electrocatalytic Activity in Metallic Thin Films through Surface Segregation of Carbon *Phys. Chem. Chem. Phys.* 2024 DOI: 10.1039/D3CP04316A.
(12) Gao, J.; Zhong, J.; Bai, L.; Liu, J.; Zhao, G.; Sun, X. Revealing the Role of Catalysts in Carbon Nanotubes and Nanofibers by Scanning Transmission X-Ray Microscopy. *Sci. Rep.* **2014**, *4* (1), No. 3606.
(13) He, K. N.; Kong, X. S.; Liu, C. S. Robust Activation Energy Predictions of Solute Diffusion from Machine Learning Method. *Comput. Mater. Sci.* **2020**, *184*, No. 109948.
(14) Weng, W.; Biesiekierski, A.; Li, Y.; Wen, C. Effects of Selected Metallic and Interstitial Elements on the Microstructure and Mechanical Properties of Beta Titanium Alloys for Orthopedic Applications. *Materialia* **2019**, *6*, No. 100323.
(15) Chen, T.; Foo, C.; Tsang, S. C. E. Interstitial and Substitutional Light Elements in Transition Metals for Heterogeneous Catalysis. *Chem. Sci.* **2021**, *12* (2), 517−532.
(16) Young, D. J. Simultaneous Oxidation and Carburisation of Chromia Forming Alloys. *Int. J. Hydrogen Energy* **2007**, *32* (16), 3763−3769.
(17) Pande, I.; Pascual, L. F.; Kousar, A.; Peltola, E.; Jiang, H.; Laurila, T. Interface Matters-Effects of Catalyst Layer Metallurgy on Macroscale Morphology and Electrochemical Performance of Carbon Nanofiber Electrodes. *Diamond Relat. Mater.* **2023**, *131*, No. 109566.
(18) Wagner, C. D.; Naumkin, A. V.; Kraut-Vass, A.; Allison, J. W.; Powell, C. J.; Rumble Jr, J. R. NIST X-Ray Photoelectron Spectroscopy Database, NIST Standard Reference Database 20, Version 3.5. (retrieved July 20, 2023) http://srdata.nist.gov/xps/Default.aspx.
(19) Arstila, K.; Julin, J.; Laitinen, M. I.; Aalto, J.; Konu, T.; Kärkkäinen, S.; Rahkonen, S.; Raunio, M.; Itkonen, J.; Santanen, J.-P.; et al. Potku–New Analysis Software for Heavy Ion Elastic Recoil Detection Analysis. *Nucl. Instrum. Methods Phys. Res., Sect. B* **2014**, *331*, 34−41.
(20) Biesinger, M. C.; Lau, L. W. M.; Gerson, A. R.; Smart, R. S. C. Resolving Surface Chemical States in XPS Analysis of First Row Transition Metals, Oxides and Hydroxides: Sc, Ti, V, Cu and Zn. *Appl. Surf. Sci.* **2010**, *257* (3), 887−898.
(21) Biesinger, M. C.; Payne, B. P.; Lau, L. W. M.; Gerson, A.; Smart, R. S. C. X-Ray Photoelectron Spectroscopic Chemical State Quantification of Mixed Nickel Metal, Oxide and Hydroxide Systems. *Surf. Interface Anal.* **2009**, *41* (4), 324−332.
(22) Susi, T.; Pichler, T.; Ayala, P. X-Ray Photoelectron Spectroscopy of Graphitic Carbon Nanomaterials Doped with Heteroatoms. *Beilstein J. Nanotechnol.* **2015**, *6* (1), 177−192.
(23) Okpalugo, T. I. T.; Papakonstantinou, P.; Murphy, H.; McLaughlin, J.; Brown, N. M. D. High Resolution XPS Characterization of Chemical Functionalised MWCNTs and SWCNTs. *Carbon* **2005**, *43* (1), 153−161.
(24) Aronniemi, M.; Sainio, J.; Lahtinen, J. Chemical State Quantification of Iron and Chromium Oxides Using XPS: The Effect of the Background Subtraction Method. *Surf. Sci.* **2005**, *578* (1−3), 108−123.
(25) Bullen, H. A.; Garrett, S. J. CrO2 by XPS: Comparison of CrO2 Powder to CrO2 Films on TiO2 (110) Single Crystal Surfaces. *Surf. Sci. Spectra* **2001**, *8* (3), 225−233.
(26) Tam, P. L.; Nyborg, L. Sputter Deposition and XPS Analysis of Nickel Silicide Thin Films. *Surf. Coat. Technol.* **2009**, *203* (19), 2886−2890.
(27) Lee, S.-H.; Cheong, H. M.; Park, N.-G.; Tracy, C. E.; Mascarenhas, A.; Benson, D. K.; Deb, S. K. Raman Spectroscopic Studies of Ni–W Oxide Thin Films. *Solid State Ionics* **2001**, *140* (1−2), 135−139.
(28) Mohammadtaheri, M.; Yang, Q.; Li, Y.; Corona-Gomez, J. The Effect of Deposition Parameters on the Structure and Mechanical Properties of Chromium Oxide Coatings Deposited by Reactive Magnetron Sputtering. *Coatings* **2018**, *8* (3), 111.
(29) Baranov, A. V.; Bogdanov, K. V.; Fedorov, A. V.; Yarchuk, M. V.; Ivanov, A. I.; Veiko, V. P.; Berwick, K. Micro-Raman Characterization of Laser-Induced Local Thermo-Oxidation of Thin Chromium Films. *J. Raman Spectrosc.* **2011**, *42* (9), 1780−1783.
(30) Kumar, R.; Sahu, G.; Saxena, S. K.; Rai, H. M.; Sagdeo, P. R. Qualitative Evolution of Asymmetric Raman Line-Shape for Nanostructures. *Silicon* **2014**, *6*, 117−121.
(31) Casiraghi, C.; Ferrari, A. C.; Robertson, J. Raman Spectroscopy of Hydrogenated Amorphous Carbons. *Phys. Rev. B* **2005**, *72* (8), 085401.
(32) Kassab, L. R.; Santos, A. D.; Pillis, M. F. Evaluation of Carbon Thin Films Using Raman Spectroscopy. *Mater. Res.* **2018**, *21* (4), No. e20170787.
(33) Ferrari, A. C. Raman Spectroscopy of Graphene and Graphite: Disorder, Electron–Phonon Coupling, Doping and Nonadiabatic Effects. *Solid State Commun.* **2007**, *143* (1−2), 47−57.
(34) Zhao, T.; Xu, C.; Ma, W.; Liu, Z.; Zhou, T.; Liu, Z.; Feng, S.; Zhu, M.; Kang, N.; Sun, D.-M.; et al. Ultrafast Growth of Nanocrystalline Graphene Films by Quenching and Grain-Size-Dependent Strength and Bandgap Opening. *Nat. Commun.* **2019**, *10* (1), No. 4854.
(35) Lubas, M.; Jasinski, J. J.; Sitarz, M.; Kurpaska, L.; Podsiad, P.; Jasinski, J. Raman Spectroscopy of TiO2 Thin Films Formed by Hybrid Treatment for Biomedical Applications. *Spectrochim. Acta, Part A* **2014**, *133*, 867−871.
(36) Sui, L.; Wu, T.; Liu, L.; Wang, H.; Wang, Q.; Hou, H.; Guo, Q. A Sensitive Pyrimethanil Sensor Based on Electrospun TiC/C Film. *Sensors* **2019**, *19* (7), 1531.
(37) Alidokht, S. A.; Munagala, V. N. V.; Chromik, R. R. Role of Third Bodies in Friction and Wear of Cold-Sprayed Ti and Ti–TiC Composite Coatings. *Tribol. Lett.* **2017**, *65*, 114.
(38) Donthu, S. K.; Chi, D. Z.; Tripathy, S.; Wong, A. S. W.; Chua, S. J. Micro-Raman Spectroscopic Investigation of NiSi Films Formed on BF 2+-, B+-and Non-Implanted (100) Si Substrates. *Appl. Phys. A* **2004**, *79*, 637−642.
(39) Finger, L. W.; Hazen, R. M. Crystal Structure and Isothermal Compression of Fe2O3, Cr2O3, and V2O3 to 50 Kbars. *J. Appl. Phys.* **1980**, *51* (10), 5362−5367.
(40) Wang, Z.; Xi, L.; Yang, Y.; Li, Y.; Han, X.; Zuo, Y.; Wang, J. Spin-Dependent Transport Properties of CrO 2 Micro Rod. *Nano-Micro Lett.* **2014**, *6*, 365−371.
(41) Qin, W.; Volinsky, A. A.; Werho, D.; Theodore, N. D.; Kottke, M.; Ramiah, C. Spontaneous Oxide Reduction in Metal Stacks. *Thin Solid Films* **2005**, *473* (2), 236−240.
(42) Pang, X.; Gao, K.; Yang, H.; Qiao, L.; Wang, Y.; Volinsky, A. A. Interfacial Microstructure of Chromium Oxide Coatings. *Adv. Eng. Mater.* **2007**, *9* (7), 594−599.
(43) Wood, I. G.; Ahmed, J.; Dobson, D. P.; Vočadlo, L. High-Pressure Phase Transitions and Equations of State in NiSi. III. A New High-Pressure Phase of NiSi. *J. Appl. Crystallogr.* **2013**, *46* (1), 14−24.

(44) Banfield, J. F.; Veblen, D. R.; Smith, D. J. The Identification of Naturally Occurring TiO2 (B) by Structure Determination Using High-Resolution Electron Microscopy, Image Simulation, and Distance-Least-Squares Refinement. *Am. Mineral.* **1991**, *76* (3−4), 343−353.
(45) Saba, F.; Zhang, F.; Liu, S.; Liu, T. Reinforcement Size Dependence of Mechanical Properties and Strengthening Mechanisms in Diamond Reinforced Titanium Metal Matrix Composites. *Composites, Part B* **2019**, *167*, 7−19.
(46) Velikanova, T. Y.; Bondar, A. A.; Grytsiv, A. V. The Chromium-Nickel-Carbon (Cr-Ni-C) Phase Diagram. *J. Phase Equilib.* **1999**, *20* (2), 125−147.
(47) Li, J.; Li, P.; Li, J.; Tian, Z.; Yu, F. Highly-Dispersed Ni-NiO Nanoparticles Anchored on an SiO2 Support for an Enhanced CO Methanation Performance. *Catalysts* **2019**, *9* (6), 506.
(48) Arif, A. F.; Balgis, R.; Ogi, T.; Iskandar, F.; Kinoshita, A.; Nakamura, K.; Okuyama, K. Highly Conductive Nano-Sized Magnéli Phases Titanium Oxide (TiOx). *Sci. Rep.* **2017**, *7* (1), No. 3646.
(49) Sen, W.; Sun, H.; Yang, B.; Xu, B.; Ma, W.; Liu, D.; Dai, Y. Preparation of Titanium Carbide Powders by Carbothermal Reduction of Titania/Charcoal at Vacuum Condition. *Int. J. Refract. Met. Hard Mater.* **2010**, *28* (5), 628−632.
(50) Li, G. Y.; Li, X.; Chen, Z.; Wang, J.; Wang, H.; Che, R. Large Areas of Centimeters-Long SiC Nanowires Synthesized by Pyrolysis of a Polymer Precursor by a CVD Route. *J. Phys. Chem. C* **2009**, *113* (41), 17655−17660.
(51) Mao, Z.; Kim, Y.-C.; Lee, H.-D.; Adusumilli, P.; Seidman, D. N. NiSi Crystal Structure, Site Preference, and Partitioning Behavior of Palladium in NiSi (Pd)/Si (100) Thin Films: Experiments and Calculations. *Appl. Phys. Lett.* **2011**, *99* (1), No. 013106.
(52) Hossain, M. D.; Zhang, Q.; Cheng, T.; Goddard, W. A., III; Luo, Z. Graphitization of Low-Density Amorphous Carbon for Electrocatalysis Electrodes from ReaxFF Reactive Dynamics. *Carbon* **2021**, *183*, 940−947.
(53) Gibot, P. Centimetric-Sized Chromium (III) Oxide Object Synthesized by Means of the Carbon Template Replication. *Ceramics* **2020**, 3 (1), 92−100.
(54) Kumar, U. N.; Malek, A.; Rao, G. R.; Thomas, T. Chromium Oxynitride (CrON) Nanoparticles: An Unexplored Electrocatalyst for Oxygen Evolution Reaction. *Electrocatalysis* **2022**, *13*, 62−71.
(55) Mikulik, D.; Ricci, M.; Tutuncuoglu, G.; Matteini, F.; Vukajlovic, J.; Vulic, N.; Alarcon-Llado, E.; i Morral, A. F. Conductive-Probe Atomic Force Microscopy as a Characterization Tool for Nanowire-Based Solar Cells. *Nano Energy* **2017**, *41*, 566−572.
(56) Azam, R. M.The Study of Chromium Nitride Coating by Asymmetric Bipolar Pulsed DC Reactive Magnetron Sputtering *Doctoral Dissertation, Lappeenranta University of Technology* 2017, pp 41−44.
(57) Otsuka, K.; Ren, X. Martensitic Transformations in Nonferrous Shape Memory Alloys. *Mater. Sci. Eng. A* **1999**, *273-275*, 89−105.
(58) Todankar, B.; Desai, P.; Ranade, A. K.; Narayanan, T. N.; Tanemura, M.; Kalita, G. Trifunctional Electrocatalytic Activities of Nitrogen-Doped Graphitic Carbon Nanofibers Synthesized by Chemical Vapor Deposition. *ChemistrySelect* **2021**, *6* (20), 4867−4873.
(59) Todankar, B.; Yaakob, Y.; Kalita, G.; Tanemura, M. Electrochemical Reactivity Investigation of Urea Oxidation Reaction in Nichrome/Nitrogen Doped Carbon Nanofibers Synthesized by CVD Method. *ChemistrySelect* **2022**, *7* (26), No. e202201386.
(60) Davies, H.; Smeltzer, W. W. Oxygen and Metal Activities of the Chromium-Nickel-Oxygen System between 900 and 1100 C. *J. Electrochem. Soc.* **1974**, *121* (4), 543.
(61) Wolf, I.; Grabke, H. J. A Study on the Solubility and Distribution of Carbon in Oxides. *Solid State Commun.* **1985**, *54* (1), 5−10.
(62) Xia, C.; Yanjun, X.; Ning, W. Facile Synthesis of NiO Nanoflowers and Their Electrocatalytic Performance. *Sens. Actuators, B* **2011**, *153* (2), 434−438.
(63) Shu, Y.; Lu, Q.; Yuan, F.; Tao, Q.; Jin, D.; Yao, H.; Xu, Q.; Hu, X. Stretchable Electrochemical Biosensing Platform Based on Ni-MOF Composite/Au Nanoparticle-Coated Carbon Nanotubes for Real-Time Monitoring of Dopamine Released from Living Cells. *ACS Appl. Mater. Interfaces* **2020**, *12* (44), 49480−49488.
(64) Jahani, S.; Beitollahi, H. Selective Detection of Dopamine in the Presence of Uric Acid Using NiO Nanoparticles Decorated on Graphene Nanosheets Modified Screen-Printed Electrodes. *Electroanalysis* **2016**, *28* (9), 2022−2028.
(65) Bertel, L.; Miranda, D. A.; García-Martín, J. M. Nanostructured Titanium Dioxide Surfaces for Electrochemical Biosensing. *Sensors* **2021**, *21* (18), 6167.
(66) Guo, Q.; Wu, T.; Liu, L.; Hou, H.; Chen, S.; Wang, L. Flexible and Conductive Titanium Carbide–Carbon Nanofibers for the Simultaneous Determination of Ascorbic Acid, Dopamine and Uric Acid. *J. Mater. Chem. B* **2018**, *6* (28), 4610−4617.
(67) Froes, Fh. *Titanium: Physical Metallurgy, Processing, and Applications*; ASM international, 2015.
(68) Lütjering, G.; Williams, J. C. *Titanium*; Springer, 2007; pp 367−382.
(69) Gusev, A. I. Phase Equilibria, Phases and Compounds in the Ti–C System. *Russ. Chem. Rev.* **2002**, *71* (6), 439−463.
(70) Szkliniarz, A.; Szkliniarz, W. Carbon in Commercially Pure Titanium. *Materials* **2023**, *16* (2), 711.
(71) Bandyopadhyay, D.; Sharma, R. C.; Chakraborti, N. The Ti-Ni-C System (Titanium-Nickel-Carbon). *J. Phase Equilib.* **2000**, *21* (2), 186.
(72) Qiu, A.-T.; Liu, L.-J.; Wei, P.; Lu, X.-G.; Li, C.-H. Calculation of Phase Diagram of Ti-Ni-O System and Application to Deoxidation of TiNi Alloy. *Trans. Nonferrous Met. Soc. China* **2011**, *21* (8), 1808−1816.
(73) Hu, B.; Yuan, X.; Du, Y.; Wang, J.; Liu, Z.-K. Thermodynamic Reassessment of the Ni–Si–Ti System Using a Four-Sublattice Model for Ordered/Disordered Fcc Phases Supported by First-Principles Calculations. *J. Alloys Compd.* **2017**, *693*, 344−356.
(74) Cao, Z.; Xie, W.; Jung, I.-H.; Du, G.; Qiao, Z. Critical Evaluation and Thermodynamic Optimization of the Ti-CO System and Its Applications to Carbothermic TiO 2 Reduction Process. *Metall. Mater. Trans. B* **2015**, *46*, 1782−1801.

https://doi.org/10.1021/acs.jpcc.3c07221
J. Phys. Chem. C 2024, 128, 1457−1468